J|A|C|S

JOURNAL OF THE AMERICAN CHEMICAL SOCIETY

pubs.acs.org/JACS

Article

Direct Imaging of Correlated Defect Nanodomains in a Metal–Organic Framework

Duncan N. Johnstone,* Francesca C. N. Firth, Clare P. Grey, Paul A. Midgley, Matthew J. Cliffe, and Sean M. Collins*

Read Online

ACCESS | Metrics & More | Article Recommendations | Supporting Information

ABSTRACT: Defect engineering can enhance key properties of metal–organic frameworks (MOFs). Tailoring the distribution of defects, for example in correlated nanodomains, requires characterization across length scales. However, a critical nanoscale characterization gap has emerged between the bulk diffraction techniques used to detect defect nanodomains and the subnanometer imaging used to observe individual defects. Here, we demonstrate that the emerging technique of scanning electron diffraction (SED) can bridge this gap uniquely enabling both nanoscale crystallographic analysis and the low-dose formation of multiple diffraction contrast images for defect analysis in MOFs. We directly image defect nanodomains in the MOF UiO-66(Hf) over an area of ca. 1000 nm and with a spatial resolution ca. 5 nm to reveal domain morphology and distribution. Based on these observations, we suggest possible crystal growth processes underpinning synthetic control of defect nanodomains. We also identify likely dislocations and small angle grain boundaries, illustrating that SED could be a key technique in developing the potential for engineering the distribution of defects, or "microstructure", in functional MOF design.
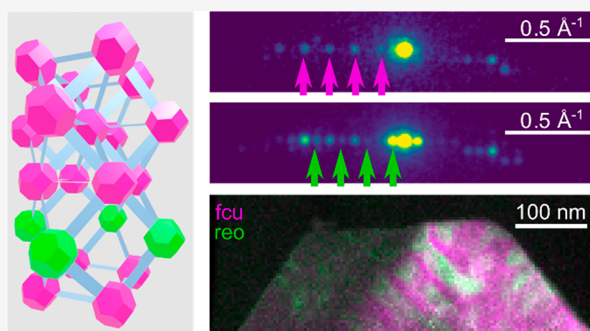
INTRODUCTION

Synthetic control of property-determining defects and the distribution of these defects in crystalline materials (i.e., microstructure) enables "defect engineering" of specific functionality in metal organic frameworks (MOFs).[1,2] MOFs comprise metal ions or clusters connected in a network by organic ligands or linkers. Missing linker or missing metal cluster defects augment MOF porosity and introduce open metal sites, improving gas storage, separation, and catalytic performance.[3–5] Correlated defect nanodomains are typified by the MOF UiO-66, which contains nanoscale domains of missing metal clusters under appropriate synthesis conditions.[2,6] These nanodomains significantly enhance high-pressure gravimetric gas sorption[7] and enable tuning of negative thermal expansion.[8] Analogous correlated defect structures are exploited technologically in, for example, relaxor ferroelectrics,[9] thermoelectrics,[10] and nickel-based super-alloys.[11] However, the morphology and distribution of defect nanodomains in MOF microstructure has not been observed directly. For correlated defects, and the distribution of defects more broadly, to play a similarly significant role in functional MOF design, as in other solid-state applications, detailed structural characterization is required on length scales from the atomic to the bulk to establish structure–property relationships and develop fundamental understanding of defect domain formation processes.

Measurement of the bulk defect concentration in MOFs is possible via compositional analysis using, for example, thermogravimetric analysis and NMR spectroscopy of digested solutions.[4,12] These methods yield the ensemble average defect concentration[13,14] but offer no information regarding the local defect arrangement.[2] The relative distribution of defects and their local chemical environment has been obtained in a variety of defective MOFs through bulk spectroscopic techniques such as FTIR,[15] NMR,[16] and EXAFS,[13] as well as total scattering X-ray diffraction methods probing correlated disorder.[6] While these spectroscopic and diffraction techniques provide information regarding local defect arrangement in the ensemble average, they do not offer direct spatially resolved measurement of how the defect distribution may change throughout the sample. Spatially resolved techniques such as confocal fluorescence microscopy,[17] fluorescence lifetime imaging,[18] and atomic force microscopy[19] have revealed defect structures in microscopic detail but have been limited to ca. 200 nm diffraction limited spatial resolution or have been

constrained to the use of fluorescent tags or to the surfaces of particles. These important techniques therefore provide limited direct evidence for defect distribution on the atomic- and nanoscale.

Transmission electron microscopy (TEM) offers the spatial resolution for atomic- and nanoscale defect characterization but MOFs typically undergo significant damage under a low cumulative electron fluence ca. 10−20 e⁻ Å⁻².[20] Such damage may be avoided by using low-dose electron microscopy techniques, which have recently been pushed forward by the development of direct electron detectors. These developments have allowed MOFs and other beam sensitive materials to be studied in various new ways. For example, 3D electron diffraction (3D-ED) has been used to achieve direct structure solution, similar to single crystal X-ray diffraction, from individual microcrystals of MOFs,[21,22] microporous zeolites,[23] and covalent organic frameworks.[24] However, while analysis of diffuse scattering in 3D-ED data has revealed stacking disorder and twinning,[23,25] this technique does not offer spatially resolved characterization below the scale of a particle. High-resolution (HR) TEM imaging can provide subparticle defect characterization,[26−28] and direct electron detection has enabled HRTEM imaging of individual defects[3] as well as the atomic structure at grain boundaries and surfaces.[20,29] However, HRTEM requires thin (<ca. 100 nm) samples, restricting the technique to the study of nanoscale MOF particles or thin edges of larger MOF particles, and the field of view at high magnification is usually restricted to ca. 20 nm. Direct observation of the defect and crystal phase distribution at lengths ca. 20−500 nm has therefore not yet been possible in MOFs. This has limited insights into the morphology, orientation, and distribution of defect nanodomains as well as other extended defects.

Diffraction contrast TEM is a powerful method of defect analysis across the nanoscale characterization gap between other techniques but has rarely been applied to MOFs.[30] Conventional diffraction contrast TEM involves introducing a physical aperture into the back-focal plane of the imaging lens, where a diffraction pattern is formed, to obtain an image using a single diffracted beam (dark-field) or the direct beam (bright-field). The image contrast results from changes in the diffracted beam intensity, typically due to differences in orientation of crystals in the field of view, due to the distortion of corresponding atomic planes around defects, or due to changes in the structure factor caused by correlated defects. Multiple images, recorded at different diffraction conditions or using different diffracted beams, are usually required for a full defect analysis. The application of such imaging to MOFs is particularly challenging because commercially available apertures are typically too large to select only one diffracted beam for materials with such large unit cells (ca. 20 Å) and because aligning the specimen to multiple diffraction conditions is limited by beam sensitivity. Here, we overcome these challenges using the emerging TEM-based technique of scanning electron diffraction (SED) performed with an electron-counting type direct electron detector to obtain rich data using a low electron fluence of ca. 5 e⁻ Å⁻² (see Methods) for both crystallographic analysis and the computational generation of numerous diffraction contrast images for defect analysis.[31]

SED is a four-dimensional scanning transmission electron microscopy (4D-STEM) technique[32] in which a two-dimensional diffraction pattern is acquired at each position as a

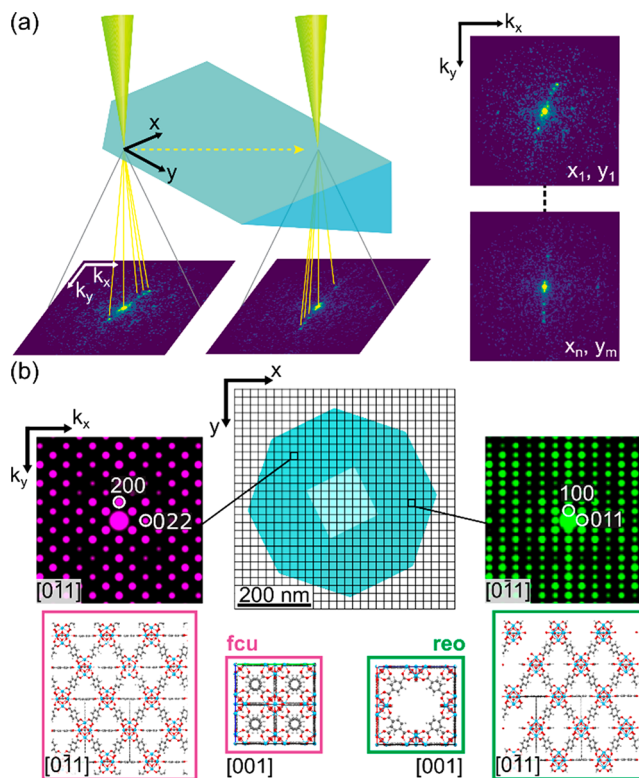focused electron probe is scanned across the sample, as in Figure 1a. The use of a highly parallel probe (ca. 1 mrad

Figure 1. Illustration of scanning electron diffraction (SED) applied to a defect-engineered UiO-66(Hf) particle. (a) A 2D (k_x, k_y) diffraction pattern is recorded in transmission at every probe position in a 2D (x, y) scan. (b) Calculated 4D-SED for a defective UiO-66(Hf) octahedral particle (blue) containing defect nanodomains and imaged along the [0$\bar{1}$1] zone axis. Where the defect-free **fcu** structure occurs (magenta), only "parent reflections" (hkl) where h, k, and l are either all even or all odd integers are measured in the [0$\bar{1}$1] zone axis diffraction pattern. Within defect nanodomains where the defective **reo** structure occurs (green), "superlattice reflections" (hkl) where h, k, and l are a mixture of odd and even integers, are also measured in the [0$\bar{1}$1] zone axis diffraction pattern. These superlattice reflections are used to identify the **reo** defect nanodomains and are observed because missing metal cluster vacancies in the defective **reo** phase change the lattice type from cubic-F (**fcu**) to cubic-P (**reo**). These vacancies are visualized clearly in the [001] projection of the structure and are visible in the [0$\bar{1}$1] projections associated with the diffraction patterns shown.

convergence angle) enables crystallographic analysis of separated Bragg disks but limits the electron probe size, and consequently the spatial resolution, to ca. 2−5 nm. Scanning yields spatially resolved diffraction data over a field of view of ca. 1 000 nm, ideal for characterizing nanoscale defect domains. SED has recently been applied to characterize correlated defects, for example, using the symmetry within individual convergent beam diffraction disks to map domains in relaxor ferroelectrics,[33] superlattice reflections as signatures of correlated disorder in meteorites,[34] and dark-field imaging to resolve monoclinic variants in transition metal oxides.[35] Further, SED has been applied to beam sensitive materials revealing crystallinity in organic molecular crystals,[36] polymers,[37] halide perovskites,[38] and MOFs.[39,40] Here, we apply

SED to directly visualize nanoscale defect domains in UiO-66(Hf).

UiO-66(Hf) is the prototypical system forming correlated defect domains in MOFs.[2,13] The UiO-66 structure consists of metal oxyhydroxide clusters that are coordinated by terephthalate (1,4-benzenedicarboxylate) ligands, giving rise to a net with 12 connected nodes with the **fcu** topology and the nominal formula $[M_6O_4(OH)_4][C_6H_4(COO)_2]_6$, where M = Zr, Hf, or other tetravalent metals. The UiO-66 family exhibits high chemical, thermal, and mechanical stability among MOFs[41−43] and the presence of defects in UiO-66 can be controlled by introducing competing ligands (modulators) such as monocarboxylic acids or water and varying the reaction temperatures and time,[44−46] resulting either in "linker vacancies", where the bidentate ligand is replaced by a monodentate species, or in cluster vacancies.[2,14] The defect-free **fcu** crystal structure of UiO-66 has a cubic-F lattice and so Bragg diffraction only occurs for "parent reflections" (hkl) where h, k, and l are either all odd or all even integers. At high defect concentrations, metal cluster vacancies order into correlated defect nanodomains, which consist of an 8-coordinated cubic-P defect phase with **reo** topology. The breaking of the face-centering symmetry means that the **reo** phase diffracts to additional primitive "superlattice reflections" (hkl) where h, k, and l are a mixture of both odd and even integers. The observation of these superlattice reflections, both in selected area electron diffraction (SAED) and powder X-ray diffraction (XRD) experiments, has previously demonstrated the existence of defect nanodomains in UiO-66(Hf).[6] However, the size, morphology, and local orientation of these nanodomains have remained ambiguous due the length scales probed by the characterization techniques applied to date.

In this work, we use superlattice reflections observed in SED experiments to directly image **reo** defect nanodomains in UiO-66(Hf) particles, as illustrated in Figure 1b. Our SED analysis directly reveals key details of the correlated defect microstructure including domain size, morphology, local orientation, and spatial distribution. Further, our analysis reveals inherent defects in otherwise single crystal UiO-66(Hf) octahedral particles. These insights are complementary to bulk XRD and subnanometer resolution STEM measurements that we perform on a series of UiO-66(Hf) samples with controlled defect densities. Together, our multimodal measurements convey previously hidden aspects of defect clustering and establish crucial experimental evidence for understanding crystal growth in defect engineered MOFs.

■ RESULTS AND DISCUSSION

We prepared a series of defective UiO-66(Hf) powders with synthetically controlled missing metal cluster defects by using formic acid as a modulator during synthesis and altering the molar ratio of $HfCl_4$ to terephthalic acid (H_2BDC) to obtain different defect densities.[4,6] Four samples were produced with $HfCl_4$:H_2BDC molar ratios of 6:5, 1:1, 3:4, and 3:5 in order of decreasing defect density. Hereafter, we refer to samples in this series as n(Hf):m(BDC) UiO-66, where n and m define the molar ratio of precursors in the reaction mixture without necessarily implying the metal:linker ratio in the product. This synthesis primarily produced octahedral particles for all defect densities as observed in scanning electron microscopy (SEM) images (Figure S1).

SED data obtained from all four defective UiO-66(Hf) samples were used to perform crystallographic analysis and to form numerous images *post facto*. Annular dark field (ADF) images were produced by plotting the integrated diffraction signal in an annular range as a function of probe position (see Methods). Such an ADF image of a typical octahedral particle of the most defective 6(Hf):5(BDC) UiO-66 material is shown in Figure 2a. Electron diffraction patterns from selected regions
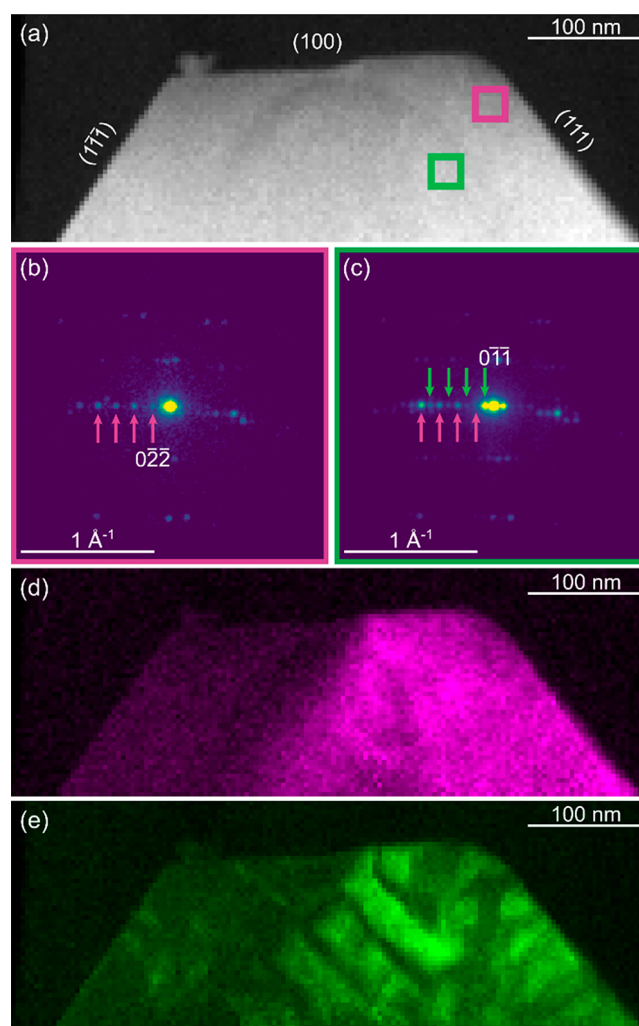

Figure 2. SED analysis of defect nanodomains in a 6(Hf):5(BDC) UiO-66(Hf) particle with high defect density. (a) ADF-STEM image indicating regions where integrated electron diffraction patterns (b, c) were selected. (b) Diffraction pattern from the magenta region, marked in in a, containing only parent reflections indicating the **fcu** phase. (c) Diffraction pattern from the green region, marked in a, containing both parent and superlattice reflections indicating the **reo** phase. (d) VDF image formed using integration windows centered on the parent reflections, marked in b. (e) VDF image formed using integration windows centered on superlattice reflections, marked in c, to directly image **reo** defect nanodomains.

of this particle, isolated computationally from the SED data set, are shown in Figure 2b−c. Bragg reflections are observed beyond 1 Å⁻¹ resolution indicating that significant electron beam induced damage was avoided. Both diffraction patterns shown in Figure 2b-c contain an 011 systematic row of reflections and have been recorded near, but not exactly at, the [0$\bar{1}$1] zone axis. These patterns therefore contain many of the

same reflections as illustrated in Figure 1b. The observation of similar diffraction patterns from both the **fcu** and **reo** phases shows that the crystallographic axes of these phases are aligned and share characteristic planar interfaces. Further, the observation of both phases within the same particle, definitively rules out the possibility of phase pure **reo** nanoparticles having formed instead using only the SED data. By comparing particle morphology observed in the ADF image with the diffraction data from the same area, the facets were indexed as the {100} and {111} facets of a truncated octahedron, as predicted by a Wulff construction[47] (Figure 2a and Figures S2−S3).

Diffraction contrast images were formed by plotting the summed intensity within selected disk-shaped integration windows in each diffraction pattern in the SED data, as a function of probe position, to form "virtual dark field" (VDF) images.[31] The integration windows were selected to capture Bragg disks recorded at particular probe positions. VDF images were formed by summing multiple integration windows to enhance the signal-to-noise ratio and, to some extent, to integrate over small mis-orientations across the field of view (see Methods for further details). Superlattice reflections (unique to the **reo** defect phase) were observed only in some regions of the most defective 6(Hf):5(BDC) UiO-66(Hf) particle (Figure 2b-c), whereas parent reflections (measured from both **fcu** and **reo** phases) were observed across the whole particle, as expected. We note that, in contrast to our XRD measurements where superlattice peaks are broadened, the superlattice reflections measured in SED are comparably sharp relative to the parent reflections because the defect domains are larger than the electron probe size. A VDF image formed using the parent reflections (marked in Figure 2b) is shown in Figure 2d and reveals a continuous region, indicating a slightly deformed crystal, on the right side of the particle. A VDF image for the **reo**-specific superlattice reflections is shown in Figure 2e, revealing rectangular domains in a lamellar structure of **reo** and **fcu** material. The largest rectangular domains have a short dimension of <50 nm and a long dimension of >100 nm. The domains appear to be preferentially orientated with the long axis of the domain perpendicular to a particle facet. We note that domains are imaged in projection in SED and are only observed if they are in a suitable orientation for Bragg diffraction. As such, VDF images outline two dimensions of the three-dimensional defect domains and domains that are not aligned with the orientation of the parent particle will not be detected in this near zone axis configuration. Our observations are therefore consistent with prior studies showing that the **reo** defect domains are epitaxial with the **fcu** structure.[3,6] Studying multiple particles likely captures the characteristic features of the domains given the high symmetry of the octahedral particles. Overlap of multiple domains in projection cannot be ruled out, and some domain sizes may appear larger as a result. We therefore complement our VDF imaging with domain size estimates from XRD measurements of the ensemble, as below. Additional examples of defect nanodomains observed by SED are presented in Figures S6−S9 with consistent observations of elongated aspect ratios highlighted in Figure S10.

The left side of the particle appears dark in Figure 2d−e, indicating a change in crystal orientation. Indexing diffraction patterns from each side of the particle (see Figure 3) shows that both sides are near to the $[0\bar{1}1]$ zone axis, suggesting only a small (<3°) change in the orientation. VDF images formed using the parent **fcu** reflections recorded on each side of the
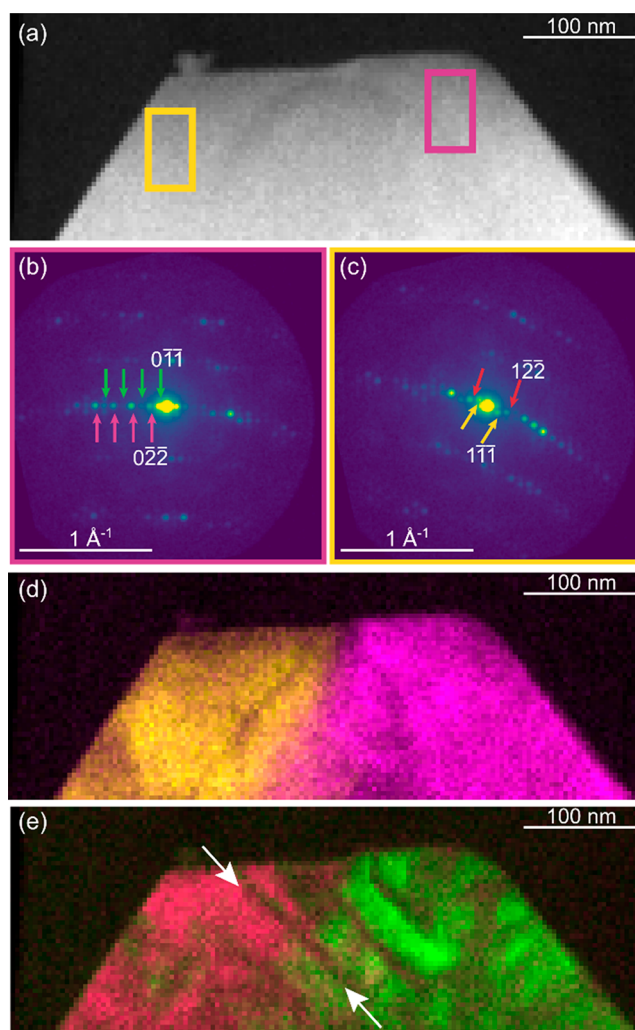

Figure 3. SED analysis of a 6(Hf):5(BDC) UiO-66(Hf) particle with high defect density, containing a grain boundary. (a) ADF-STEM image indicating regions, containing both **fcu** and **reo** phases, where integrated electron diffraction patterns (b, c) were selected in magenta and yellow. Diffraction patterns from the regions marked in (a), which contain both parent and superlattice reflections, reveal a change in orientation between the left- and right-hand side of the particle. (d) Composite VDF image formed using integration windows centered on parent reflections, magenta in b and yellow in c, revealing a small change in orientation across a boundary. (e) Composite VDF image formed using integration windows centered on superlattice reflections, green in b and red in c, revealing **reo** defect domains. Arrows in e indicate a continuous domain across the small angle boundary.

particle (Figure 3d) allow us to map the distribution of the two orientations and reveal the presence of a small angle grain boundary. Such a small angle grain boundary could be formed by an arrangement of inherent dislocations, which have been observed in other MOFs[17,19] but not previously detected in UiO-66. Using superlattice **reo** reflections $\{1\bar{2}\bar{2}\}$ on either side of the grain boundary to produce VDF images, we were able to observe how defect domains extend across this boundary (Figure 3e). We find that many defect domains are continuous across the grain boundary despite the small change in crystal orientation. However, the observation that some domains are not continuous across the boundary suggests that this interface emerged during synthesis. The presence of these micro-

structural features highlights deviations from pristine single crystal growth.

Our direct observations of the orientation, size, and morphology of defect domains in 6(Hf):5(BDC) UiO-66 were contextualized using XRD analysis of our series of defective UiO-66(Hf) samples (Figures 4 and S4−S5 and
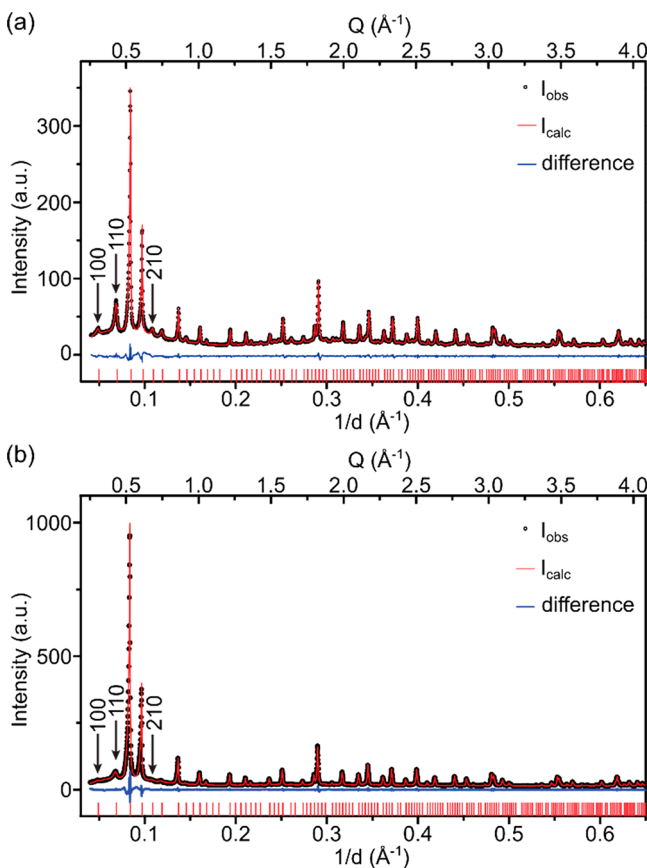

Figure 4. Powder X-ray diffraction of defective UiO-66(Hf). Pawley fitting of powder XRD data from two defective UiO-66(Hf) samples. The more defective 6(Hf):5(BDC) UiO-66(Hf) material, as in a, shows stronger superlattice reflections corresponding to the **reo** phase, e.g. 100, 110, and 210 (marked with arrows) as compared with less defective 3(Hf):4(BDC) UiO-66(Hf) material, as in b.

Table S1). Pawley refinement with a *hkl*-dependent isotropic size-broadening produced a refined domain size of 51.6 ± 1.6 nm for the 6(Hf):5(BDC) UiO-66(Hf) sample, as shown in Figure 4a. This domain size estimate is remarkably consistent with those observed in Figures 2−3. XRD analysis of the less defective 3(Hf):4(BDC) UiO-66(Hf) sample yielded a Pawley-refined domain size 31 ± 5 nm, as shown in Figure 4b. SED analysis of this less defective sample is presented in Figure 5, and a VDF image formed using superlattice reflections (Figure 5e) reveals that the **reo** domains are similar but smaller and less coherent, with sizes consistent with those estimated from XRD. The VDF image formed using parent reflections (Figure 5d) shows both sharp changes in the diffraction contrast producing a V-shape structure resembling diffraction contrast from dislocations, and an intensity modulation with a pitch ca. 50 nm that we attribute to intensity change with thickness. Further analysis of other samples in our series of defective UiO-66(Hf) samples (see Figures S6−S9) confirmed the trend that defect domain size
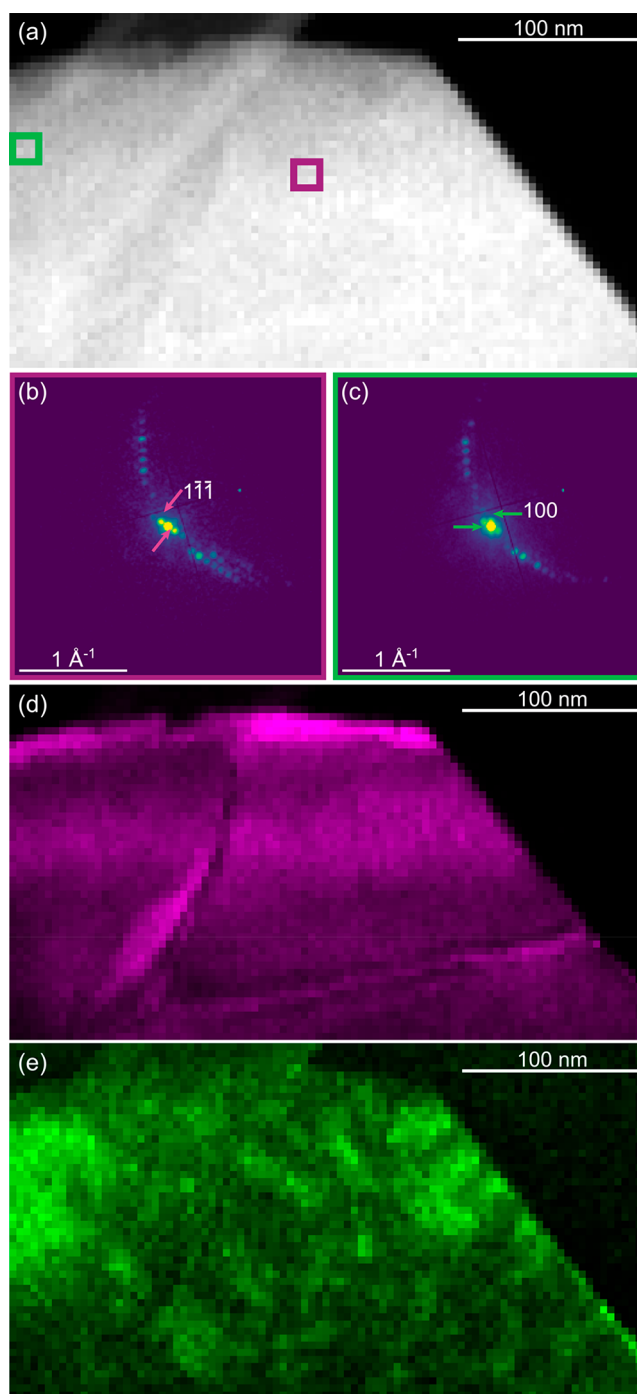

Figure 5. SED analysis of a 3(Hf):4(BDC) UiO-66(Hf) particle with reduced defect density. (a) ADF-STEM image indicating regions where integrated electron diffraction patterns (b, c) were selected. (b) Diffraction pattern from magenta region in a containing only parent reflections indicating the **fcu** phase. (c) Diffraction pattern from green region in a containing both parent and superlattice reflections indicating the **reo** phase. (d) VDF image formed using integration windows centered on the parent reflections, marked in b, revealing V-shaped defect contrast. (e) VDF image formed using integration windows centered on the superlattice reflections, marked in c, to directly image **reo** defect domains.

increases and becomes more blocky in morphology as defect concentration increases. As the fraction of the bulk powder analyzed by SED is inevitably small, multimodal diffraction studies are crucial to produce a validated model. In this case,

SED directly visualizes the **reo** domain and extended defect characteristics while the XRD analysis provides complementary information on the ensemble powder.

The blocky lamellar structure of rectangular domains observed by SED microscopy in several more defective 6(Hf):5(BDC) UiO-66(Hf) particles (Figures 2 and S6−S7), and the more fragmented but similar morphology domain structure in less defective 3(Hf):4(BDC) UiO-66(Hf) particles (Figures 5 and S8−S9) are reminiscent of phase separated microstructures produced in diffusion-limited transformations such as eutectic growth and spinodal decomposition. Previous work has demonstrated that the concentration of modulating ligands, such as formate or water, in the reaction mixture dictates the competitive formation of **reo** and **fcu**.[4−6] Our observations are consistent with local fluctuations in concentration during crystal growth controlling the local phase competition. While formate is in substantial excess, terephthalate binds more strongly. When the local concentration of terephthalate becomes sufficient to outcompete formate binding, **fcu** nucleation and growth can occur. The growth of the **fcu** phase will use up the locally available terephthalate until the local formate concentration reaches sufficient excess to outcompete the terephthalate interactions leading to **reo** growth. Further, the formation of numerous nearby **reo** and **fcu** domains of similar size and shape, and the absence of any single phase **reo** particles, points to **reo** growth colocated and in tandem with **fcu** growth. This colocalization may also be consistent with the tendency for blocky domains to be observed with the long axis of the domain perpendicular to a particle facet, which is the growth front as the particle expands. This means that the larger blocky domains could potentially be supplied with formate by short-range lateral diffusion at the growth front, like in eutectic growth. Our SED measurements therefore provide direct evidence for potential diffusion limited MOF crystal growth processes.

To examine the defect domain structure on the subnanometer scale we performed aberration-corrected bright-field (BF) STEM imaging of the 6(Hf):5(BDC) UiO-66(Hf) sample, as shown in Figure 6. The BF-STEM image (Figure 6a) was obtained near to the [0$\bar{1}$1] orientation and spatial frequencies characteristic of {100} and {011} planes of the **reo** structure are observed in the fast Fourier transform (FFT) of the BF-STEM image (Figure 6b). The BF-STEM image shows amplitude modulation along the [100] direction (Figure 6c and S11) consistent with alternating rows of metal clusters in the **reo** structure containing half the metal clusters in the column as compared with the **fcu** structure in this [0$\bar{1}$1] orientation. These image features are highlighted in the structural model presented in Figure 6c alongside a simplified schematic model of the lattice in the [0$\bar{1}$1] zone axis orientation (Figure 6d). The orientation of the defect region is consistent with our SED observations and points to cluster terminations at the particle surface, consistent with prior HRTEM studies.[3,20,29] The lattice model (Figure 6) identifies {211} planes as the likely interface on the longer sides of the rectangular **reo** domains, while there appears to be some preference for termination at {111} planes on the short dimension within UiO-66(Hf). The {211} type planes pass through metal clusters and the cluster-ligand attachment sites, which may be linked to the mechanism by which formate modulators compete with terephthalate linkers.[4−6]
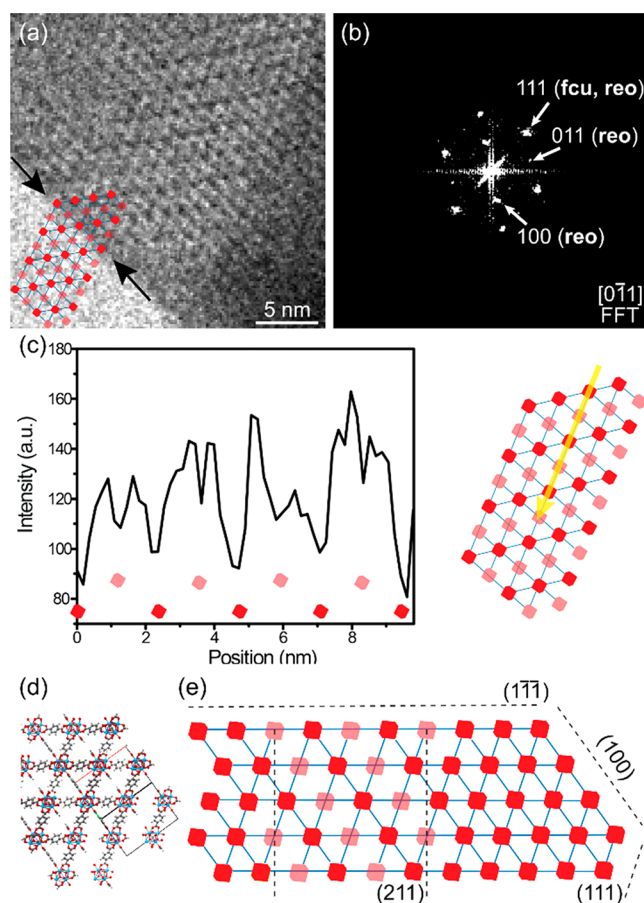

Figure 6. Lattice resolution imaging of a defect-engineered UiO-66(Hf) particle. (a) Bright-field STEM micrograph of an **reo** domain with a simplified schematic, enlarged in (c, d), overlaid. Arrows mark dark spots indicating metal clusters at the particle surface. (b) Fast Fourier transform (FFT) of the image in a with spatial frequencies marked with arrows and indexed with respect to crystal planes. (c) Line profile through bright-field STEM image alternating across columns containing one and two metal clusters per unit cell. (d) Representation of the atomic structure of the **reo** defect structure of UiO-66(Hf) in the [0$\bar{1}$1] zone axis orientation. (e) Simplified schematic of the lattice. Sites with the full or half the number of metal clusters present in the **fcu** structure are depicted as solid and transparent red projections of an octahedron, respectively.

◼ CONCLUSIONS

Our multiscale structural analysis shows that defect nanodomains in defect-engineered UiO-66(Hf) exhibit a blocky lamellar morphology and occur in a preferred orientation, extending perpendicular to {111} planes and sometimes perpendicular to other low index facets, with interfaces between **reo** and **fcu** domains on {211} planes. These characteristics remain similar across systematically varied defect densities but become more evident at high defect density. The domain size can be both controlled by synthesis and adequately inferred from XRD analysis, which are complemented by insights into the anisotropic domain morphology and distribution observed using SED. These experimental observations place previously unreported constraints on models seeking to explain defect clustering and crystal growth in MOFs, motivating further modeling of the growth kinetics to enhance understanding of synthetic control of defect structures. In particular, we suggest that the blocky

lamellar morphology may result from local fluctuations in the terephthalate concentration perpendicular to the growth direction. The serendipitous observation of inherent defects confined to the interior of the UiO-66 crystal, i.e. grain boundaries and likely dislocations, further highlighted insights that may be obtained from *post facto* analysis of the rich SED data. Together, our observations highlight the unique capabilities of SED to reveal the distribution of defects, i.e. microstructure, within MOFs based on both nanoscale crystallographic analysis and the formation of the multiple diffraction contrast images, required for a comprehensive defect analysis, using an electron fluence below the critical threshold of ca. $10-20$ e$^-$ Å^{-2}. The ability to characterize this microstructure in MOFs opens the possibility of extending the concept of defect engineering to "microstructure engineering" as a route to enhanced performance in MOFs, driven by continued development of tools for correlated defect imaging to relate defect distribution to key properties.

METHODS

Synthesis of Defective UiO-66(Hf). Samples were produced using a procedure adapted from ref 8. HfCl$_4$ (Acros Organics, 99%, 0.3 mmol, 96.1 mg) and terephthalic acid (H$_2$BDC) (Alfa Aesar, 98%, $0.25-0.5$ mmol, $41.5-83.0$ mg) were added to a 23 mL PTFE-lined steel autoclave, followed by N,N-dimethylformamide (DMF, Alfa Aesar, 99%, 4 mL), and formic acid (Fisher, 98/100%) (2.0 mL). The autoclave was sealed and heated at 150 °C for 24 h. The resulting white microcrystalline powder was filtered under vacuum, washed on the filter (DMF, 5 mL), and the solid product was dried. Unreacted ligand was removed by washing each sample with DMF (12 mL) at 60 °C for 24 h, followed by two further 2-h washing cycles. After each wash, residual DMF was removed after centrifugation of the mixture at 8000 rpm for 15 min. Finally, any residual DMF was removed by heating at 200 °C for 24 h. Four samples were produced using 0.25, 0.3, 0.4, and 0.5 mmol H$_2$BDC corresponding to HfCl$_4$:H$_2$BDC molar ratios of 6:5, 1:1, 3:4, and 3:5.

Scanning Electron Diffraction. SED data were acquired using a JEOL ARM300CF fitted with an ultrahigh-resolution pole piece, a cold field emission gun, and aberration correctors in both the probe-forming and image-forming optics (Diamond Light Source, UK). The instrument was operated at 200 kV. A nanobeam configuration was obtained by switching off the aberration corrector in the probe-forming optics and using a 10 μm condenser aperture to obtain a convergence semiangle <1 mrad and a diffraction-limited probe diameter of ca. 5 nm. The probe current was measured using a Faraday cup as ca. 2 pA, and the exposure time was 1 ms per probe position. The estimated electron fluence, assuming a disk-like probe, was ca. 5 e$^-$ Å^{-2}. A diffraction pattern was acquired at every probe position using a Merlin-Medipix hybrid counting-type direct electron detector (Quantum Detectors, UK). SED was obtained in a "blind scanning" point-and-shoot workflow to minimize the total electron fluence the specimen received. The orientation of each particle was therefore determined by the deposition of particles onto the TEM support film. Most particles were orientated near to a ⟨110⟩ zone axis due to the particle morphology. Since the **reo** reflections are prominent near the ⟨110⟩ zone axis, this particle orientation was suitable for defect analysis. This orientation also allowed facet analysis of the surfaces of truncated octahedral particles for contextualization of the defects within the crystalline particles (Figure S3).

SED data were processed using pyxem-0.10.0.[48] The diffraction patterns were aligned, rebinned, and calibrated prior to analysis (see the Supporting Information). ADF images were formed by integrating between an inner angle ($\theta_{inner} = 12.6$ mrad) and an outer angle ($\theta_{outer} = 25.6$ mrad) as a function of probe position. VDF images were obtained by manual selection of integration windows to contain Bragg disks in the whole SED data set. Initially this selection was performed using the average diffraction pattern to identify integration windows

producing VDF images that revealed the defect domain structure. Regions of interest were then manually defined within expected **reo** and **fcu** domains and area averaged diffraction patterns were extracted from these regions. The Bragg disks in these area averaged diffraction patterns were then assigned as **reo** or **fcu/reo** reflections based on pattern symmetry and validated against the measured diffraction vector magnitude. The VDFs associated with all integration windows in each category were then summed to produce VDFs less sensitive to minor variations of intensity at particular scattering vectors, as is typical due to small variations in thickness or sample orientation. All diffraction patterns shown are presented as the square-root of the recorded intensity to rebalance intensity variation between low and high angle reflections for improved visualization. This intensity scaling was applied only for visualization and not prior to the formation of VDF images. All VDF images were normalized to their respective maximum intensities when forming color overlays.

X-ray Diffraction and Pawley Refinement. Powder X-ray diffraction (PXRD) patterns were measured using a PANalytical Empyrean diffractometer (Cu Kα radiation, $\lambda = 1.541$ Å) over the 2θ range $2-60°$, using a step size of 0.017° and a scan speed of 0.020° s^{-1}. All analysis of powder diffraction data, including Pawley refinement,[49] was carried out using the TOPAS Academic 4.1 software.[50]

Pawley refinement of the PXRD data obtained from the 6(Hf):5(BDC), 1(Hf):1(BDC), and 3(Hf):4(BDC) UiO-66(Hf) samples was carried out in space group Pm$\bar{3}$m with a pseudo-Voigt peak shape and the background modeled using a freely refining Chebyshev polynomial with ten parameters. The **reo** domain size was determined by modeling the differential peak broadening between **fcu/reo**-shared Bragg peaks and **reo**-only scattering, using a crystallite-size-dependent Gaussian size-broadening term with a Scherrer-type $\cos(\theta)$ dependence Pawley refinement of the 3(Hf):5-(BDC) UiO-66(Hf) sample, which contained the lowest defect concentration, required a modified approach as the low intensity of the **reo** scattering precluded a full Pawley refinement. This refinement was carried out only on data over the 2θ range $3.5-11.0°$, and the background was restricted to a three parameter Chebyshev polynomial and a broad Gaussian peak, centered at $2\theta = 8.21(2)°$ with fwhm = 1.94(11)°. The Pawley refined lattice parameters, **reo** domain sizes, and $I\{100\}/I\{110\}$ intensity ratios are summarized in Table S1.

Scanning Transmission Electron Microscopy. Aberration corrected STEM imaging was performed using the same JEOL ARM300CF microscope as that used for SED. The instrument was operated at 300 kV, and a high condenser lens excitation and low extraction voltage was used to produce a probe current of ca. 1.8 pA with a 16 mrad convergence semiangle. BF STEM imaging was performed using a BF detector with an aperture inserted to limit the scattering angles collected to within the direct beam disk and a per pixel dwell time <20 μs.

ASSOCIATED CONTENT

ⓢ Supporting Information

The Supporting Information is available free of charge at https://pubs.acs.org/doi/10.1021/jacs.0c04468.

> Scanning electron microscopy. Scanning electron diffraction preprocessing and calibration. Particle facet indexation. Powder X-ray diffraction and Pawley refinement. Defect nanodomain imaging examples. High-resolution scanning transmission electron microscopy image analysis (PDF)

AUTHOR INFORMATION

Corresponding Authors

Sean M. Collins − *Department of Materials Science and Metallurgy, University of Cambridge, Cambridge CB3 0FS, U.K.; School of Chemical and Process Engineering and School of*

Chemistry, University of Leeds, Leeds LS2 9JT, U.K.;
orcid.org/0000-0002-5151-6360; Email: S.M.Collins@
leeds.ac.uk

Duncan N. Johnstone − *Department of Materials Science and Metallurgy, University of Cambridge, Cambridge CB3 0FS, U.K.;* orcid.org/0000-0003-3663-3793; Email: dnj23@
cam.ac.uk

Authors

  Francesca C. N. Firth − *Department of Chemistry, University of Cambridge, Cambridge CB2 1EW, U.K.*

  Clare P. Grey − *Department of Chemistry, University of Cambridge, Cambridge CB2 1EW, U.K.;* orcid.org/0000-0001-5572-192X

  Paul A. Midgley − *Department of Materials Science and Metallurgy, University of Cambridge, Cambridge CB3 0FS, U.K.*

  Matthew J. Cliffe − *School of Chemistry, University of Nottingham, Nottingham NG7 2RD, U.K.*

Complete contact information is available at:
https://pubs.acs.org/10.1021/jacs.0c04468

Notes

The authors declare no competing financial interest.

■ ACKNOWLEDGMENTS

■ REFERENCES

(1) Fang, Z.; Bueken, B.; De Vos, D. E.; Fischer, R. A. Defect-Engineered Metal−Organic Frameworks. *Angew. Chem., Int. Ed.* **2015**, *54* (25), 7234−7254.

(2) Dissegna, S.; Epp, K.; Heinz, W. R.; Kieslich, G.; Fischer, R. A. Defective Metal-Organic Frameworks. *Adv. Mater.* **2018**, *30* (37), 1704501.

(3) Liu, L.; Chen, Z.; Wang, J.; Zhang, D.; Zhu, Y.; Ling, S.; Huang, K.-W.; Belmabkhout, Y.; Adil, K.; Zhang, Y.; Slater, B.; Eddaoudi, M.; Han, Y. Imaging Defects and Their Evolution in a Metal−Organic Framework at Sub-Unit-Cell Resolution. *Nat. Chem.* **2019**, *11* (7), 622−628.

(4) Shearer, G. C.; Chavan, S.; Bordiga, S.; Svelle, S.; Olsbye, U.; Lillerud, K. P. Defect Engineering: Tuning the Porosity and Composition of the Metal−Organic Framework UiO-66 via Modulated Synthesis. *Chem. Mater.* **2016**, *28* (11), 3749−3761.

(5) Firth, F. C. N.; Cliffe, M. J.; Vulpe, D.; Aragones-Anglada, M.; Moghadam, P. Z.; Fairen-Jimenez, D.; Slater, B.; Grey, C. P. Engineering New Defective Phases of UiO Family Metal−Organic Frameworks with Water. *J. Mater. Chem. A* **2019**, *7* (13), 7459−7469.

(6) Cliffe, M. J.; Wan, W.; Zou, X.; Chater, P. A.; Kleppe, A. K.; Tucker, M. G.; Wilhelm, H.; Funnell, N. P.; Coudert, F.-X.; Goodwin, A. L. Correlated Defect Nanoregions in a Metal−Organic Framework. *Nat. Commun.* **2014**, *5* (1), 4176.

(7) Liang, W.; Coghlan, C. J.; Ragon, F.; Rubio-Martinez, M.; D'Alessandro, D. M.; Babarao, R. Defect Engineering of UiO-66 for CO2 and H2O Uptake − a Combined Experimental and Simulation Study. *Dalton Trans* **2016**, *45* (11), 4496−4500.

(8) Cliffe, M. J.; Hill, J. A.; Murray, C. A.; Coudert, F.-X.; Goodwin, A. L. Defect-Dependent Colossal Negative Thermal Expansion in UiO-66(Hf) Metal−Organic Framework. *Phys. Chem. Chem. Phys.* **2015**, *17* (17), 11586−11592.

(9) Xu, G.; Zhong, Z.; Bing, Y.; Ye, Z.-G.; Shirane, G. Electric-Field-Induced Redistribution of Polar Nano-Regions in a Relaxor Ferroelectric. *Nat. Mater.* **2006**, *5* (2), 134−140.

(10) Christensen, M.; Abrahamsen, A. B.; Christensen, N. B.; Juranyi, F.; Andersen, N. H.; Lefmann, K.; Andreasson, J.; Bahl, C. R. H.; Iversen, B. B. Avoided Crossing of Rattler Modes in Thermo-electric Materials. *Nat. Mater.* **2008**, *7* (10), 811−815.

(11) Mignanelli, P. M.; Jones, N. G.; Pickering, E. J.; Messé, O. M. D. M.; Rae, C. M. F.; Hardy, M. C.; Stone, H. J. Gamma-Gamma Prime-Gamma Double Prime Dual-Superlattice Superalloys. *Scr. Mater.* **2017**, *136*, 136−140.

(12) Taddei, M.; Wakeham, R. J.; Koutsianos, A.; Andreoli, E.; Barron, A. R. Post-Synthetic Ligand Exchange in Zirconium-Based Metal−Organic Frameworks: Beware of The Defects! *Angew. Chem., Int. Ed.* **2018**, *57* (36), 11706−11710.

(13) Valenzano, L.; Civalleri, B.; Chavan, S.; Bordiga, S.; Nilsen, M. H.; Jakobsen, S.; Lillerud, K. P.; Lamberti, C. Disclosing the Complex Structure of UiO-66 Metal Organic Framework: A Synergic Combination of Experiment and Theory. *Chem. Mater.* **2011**, *23* (7), 1700−1718.

(14) Wu, H.; Chua, Y. S.; Krungleviciute, V.; Tyagi, M.; Chen, P.; Yildirim, T.; Zhou, W. Unusual and Highly Tunable Missing-Linker Defects in Zirconium Metal−Organic Framework UiO-66 and Their Important Effects on Gas Adsorption. *J. Am. Chem. Soc.* **2013**, *135* (28), 10525−10532.

(15) Donlan, E. A.; Boström, H. L. B.; Geddes, H. S.; Reynolds, E. M.; Goodwin, A. L. Compositional Nanodomain Formation in Hybrid Formate Perovskites. *Chem. Commun.* **2017**, *53* (81), 11233−11236.

(16) Kong, X.; Deng, H.; Yan, F.; Kim, J.; Swisher, J. A.; Smit, B.; Yaghi, O. M.; Reimer, J. A. Mapping of Functional Groups in Metal-Organic Frameworks. *Science* **2013**, *341* (6148), 882−885.

(17) Ameloot, R.; Vermoortele, F.; Hofkens, J.; De Schryver, F. C.; De Vos, D. E.; Roeffaers, M. B. J. Three-Dimensional Visualization of Defects Formed during the Synthesis of Metal−Organic Frameworks: A Fluorescence Microscopy Study. *Angew. Chem., Int. Ed.* **2013**, *52* (1), 401−405.

(18) Schrimpf, W.; Jiang, J.; Ji, Z.; Hirschle, P.; Lamb, D. C.; Yaghi, O. M.; Wuttke, S. Chemical Diversity in a Metal−Organic Framework Revealed by Fluorescence Lifetime Imaging. *Nat. Commun.* **2018**, *9* (1), 1−10.

(19) Shöâeè, M.; Agger, J. R.; Anderson, M. W.; Attfield, M. P. Crystal Form, Defects and Growth of the Metal Organic Framework HKUST-1 Revealed by Atomic Force Microscopy. *CrystEngComm* **2008**, *10* (6), 646−648.

(20) Zhang, D.; Zhu, Y.; Liu, L.; Ying, X.; Hsiung, C.-E.; Sougrat, R.; Li, K.; Han, Y. Atomic-Resolution Transmission Electron Microscopy of Electron Beam−Sensitive Crystalline Materials. *Science* **2018**, *359* (6376), 675−679.

(21) Wang, B.; Rhauderwiek, T.; Inge, A. K.; Xu, H.; Yang, T.; Huang, Z.; Stock, N.; Zou, X. A Porous Cobalt Tetraphosphonate Metal−Organic Framework: Accurate Structure and Guest Molecule Location Determined by Continuous-Rotation Electron Diffraction. *Chem. - Eur. J.* **2018**, *24* (66), 17429−17433.

(22) Feng, D.; Wang, K.; Su, J.; Liu, T.-F.; Park, J.; Wei, Z.; Bosch, M.; Yakovenko, A.; Zou, X.; Zhou, H.-C. A Highly Stable Zeotype

Mesoporous Zirconium Metal−Organic Framework with Ultralarge Pores. *Angew. Chem., Int. Ed.* **2015**, *54* (1), 149−154.

(23) Willhammar, T.; Sun, J.; Wan, W.; Oleynikov, P.; Zhang, D.; Zou, X.; Moliner, M.; Gonzalez, J.; Martínez, C.; Rey, F.; Corma, A. Structure and Catalytic Properties of the Most Complex Intergrown Zeolite ITQ-39 Determined by Electron Crystallography. *Nat. Chem.* **2012**, *4* (3), 188−194.

(24) Zhang, Y.-B.; Su, J.; Furukawa, H.; Yun, Y.; Gándara, F.; Duong, A.; Zou, X.; Yaghi, O. M. Single-Crystal Structure of a Covalent Organic Framework. *J. Am. Chem. Soc.* **2013**, *135* (44), 16336−16339.

(25) Feyand, M.; Mugnaioli, E.; Vermoortele, F.; Bueken, B.; Dieterich, J. M.; Reimer, T.; Kolb, U.; de Vos, D.; Stock, N. Automated Diffraction Tomography for the Structure Elucidation of Twinned, Sub-Micrometer Crystals of a Highly Porous, Catalytically Active Bismuth Metal−Organic Framework. *Angew. Chem., Int. Ed.* **2012**, *51* (41), 10373−10376.

(26) Lebedev, O. I.; Millange, F.; Serre, C.; Van Tendeloo, G.; Férey, G. First Direct Imaging of Giant Pores of the Metal−Organic Framework MIL-101. *Chem. Mater.* **2005**, *17* (26), 6525−6527.

(27) Deng, H.; Grunder, S.; Cordova, K. E.; Valente, C.; Furukawa, H.; Hmadeh, M.; Gándara, F.; Whalley, A. C.; Liu, Z.; Asahina, S.; Kazumori, H.; O'Keeffe, M.; Terasaki, O.; Stoddart, J. F.; Yaghi, O. M. Large-Pore Apertures in a Series of Metal-Organic Frameworks. *Science* **2012**, *336* (6084), 1018−1023.

(28) Feng, D.; Liu, T.-F.; Su, J.; Bosch, M.; Wei, Z.; Wan, W.; Yuan, D.; Chen, Y.-P.; Wang, X.; Wang, K.; Lian, X.; Gu, Z.-Y.; Park, J.; Zou, X.; Zhou, H.-C. Stable Metal-Organic Frameworks Containing Single-Molecule Traps for Enzyme Encapsulation. *Nat. Commun.* **2015**, *6* (1), 1−8.

(29) Zhu, Y.; Ciston, J.; Zheng, B.; Miao, X.; Czarnik, C.; Pan, Y.; Sougrat, R.; Lai, Z.; Hsiung, C.-E.; Yao, K.; Pinnau, I.; Pan, M.; Han, Y. Unravelling Surface and Interfacial Structures of a Metal−Organic Framework by Transmission Electron Microscopy. *Nat. Mater.* **2017**, *16* (5), 532−536.

(30) Wiktor, C.; Meledina, M.; Turner, S.; Lebedev, O. I.; Fischer, R. A. Transmission Electron Microscopy on Metal−Organic Frameworks − a Review. *J. Mater. Chem. A* **2017**, *5* (29), 14969−14989.

(31) Gammer, C.; Burak Ozdol, V.; Liebscher, C. H.; Minor, A. M. Diffraction Contrast Imaging Using Virtual Apertures. *Ultramicroscopy* **2015**, *155*, 1−10.

(32) Ophus, C. Four-Dimensional Scanning Transmission Electron Microscopy (4D-STEM): From Scanning Nanodiffraction to Ptychography and Beyond. *Microsc. Microanal.* **2019**, *25* (3), 563−582.

(33) Kim, K.-H.; Payne, D. A.; Zuo, J.-M. Determination of 60° Polarization Nanodomains in a Relaxor-Based Ferroelectric Single Crystal. *Appl. Phys. Lett.* **2015**, *107* (16), 162902.

(34) Einsle, J. F.; Eggeman, A. S.; Martineau, B. H.; Saghi, Z.; Collins, S. M.; Blukis, R.; Bagot, P. A. J.; Midgley, P. A.; Harrison, R. J. Nanomagnetic Properties of the Meteorite Cloudy Zone. *Proc. Natl. Acad. Sci. U. S. A.* **2018**, *115* (49), E11436−E11445.

(35) Shukla, A. K.; Ramasse, Q. M.; Ophus, C.; Kepaptsoglou, D. M.; Hage, F. S.; Gammer, C.; Bowling, C.; Gallegos, P. A. H.; Venkatachalam, S. Effect of Composition on the Structure of Lithium- and Manganese-Rich Transition Metal Oxides. *Energy Environ. Sci.* **2018**, *11* (4), 830−840.

(36) Panova, O.; Ophus, C.; Takacs, C. J.; Bustillo, K. C.; Balhorn, L.; Salleo, A.; Balsara, N.; Minor, A. M. Diffraction Imaging of Nanocrystalline Structures in Organic Semiconductor Molecular Thin Films. *Nat. Mater.* **2019**, *18* (8), 860−865.

(37) Panova, O.; Chen, X. C.; Bustillo, K. C.; Ophus, C.; Bhatt, M. P.; Balsara, N.; Minor, A. M. Orientation Mapping of Semicrystalline Polymers Using Scanning Electron Nanobeam Diffraction. *Micron* **2016**, *88*, 30−36.

(38) Doherty, T. A. S.; Winchester, A. J.; Macpherson, S.; Johnstone, D. N.; Pareek, V.; Tennyson, E. M.; Kosar, S.; Kosasih, F. U.; Anaya, M.; Abdi-Jalebi, M.; Andaji-Garmaroudi, Z.; Wong, E. L.; Madéo, J.; Chiang, Y.-H.; Park, J.-S.; Jung, Y.-K.; Petoukhoff, C. E.; Divitini, G.;

Man, M. K. L.; Ducati, C.; Walsh, A.; Midgley, P. A.; Dani, K. M.; Stranks, S. D. Performance-Limiting Nanoscale Trap Clusters at Grain Junctions in Halide Perovskites. *Nature* **2020**, *580* (7803), 360−366.

(39) Hou, J.; Ashling, C. W.; Collins, S. M.; Krajnc, A.; Zhou, C.; Longley, L.; Johnstone, D. N.; Chater, P. A.; Li, S.; Coulet, M.-V.; Llewellyn, P. L.; Coudert, F.-X.; Keen, D. A.; Midgley, P. A.; Mali, G.; Chen, V.; Bennett, T. D. Metal-Organic Framework Crystal-Glass Composites. *Nat. Commun.* **2019**, *10* (1), 2580.

(40) Ashling, C. W.; Johnstone, D. N.; Widmer, R. N.; Hou, J.; Collins, S. M.; Sapnik, A. F.; Bumstead, A. M.; Midgley, P. A.; Chater, P. A.; Keen, D. A.; Bennett, T. D. Synthesis and Properties of a Compositional Series of MIL-53(Al) Metal−Organic Framework Crystal-Glass Composites. *J. Am. Chem. Soc.* **2019**, *141* (39), 15641−15648.

(41) Wu, H.; Yildirim, T.; Zhou, W. Exceptional Mechanical Stability of Highly Porous Zirconium Metal−Organic Framework UiO-66 and Its Important Implications. *J. Phys. Chem. Lett.* **2013**, *4* (6), 925−930.

(42) Cavka, J. H.; Jakobsen, S.; Olsbye, U.; Guillou, N.; Lamberti, C.; Bordiga, S.; Lillerud, K. P. A New Zirconium Inorganic Building Brick Forming Metal Organic Frameworks with Exceptional Stability. *J. Am. Chem. Soc.* **2008**, *130* (42), 13850−13851.

(43) Jakobsen, S.; Gianolio, D.; Wragg, D. S.; Nilsen, M. H.; Emerich, H.; Bordiga, S.; Lamberti, C.; Olsbye, U.; Tilset, M.; Lillerud, K. P. Structural Determination of a Highly Stable Metal-Organic Framework with Possible Application to Interim Radioactive Waste Scavenging: Hf-UiO-66. *Phys. Rev. B: Condens. Matter Mater. Phys.* **2012**, *86* (12), 125429.

(44) Vermoortele, F.; Bueken, B.; Le Bars, G.; Van de Voorde, B.; Vandichel, M.; Houthoofd, K.; Vimont, A.; Daturi, M.; Waroquier, M.; Van Speybroeck, V.; Kirschhock, C.; De Vos, D. E. Synthesis Modulation as a Tool To Increase the Catalytic Activity of Metal− Organic Frameworks: The Unique Case of UiO-66(Zr). *J. Am. Chem. Soc.* **2013**, *135* (31), 11465−11468.

(45) Schaate, A.; Roy, P.; Godt, A.; Lippke, J.; Waltz, F.; Wiebcke, M.; Behrens, P. Modulated Synthesis of Zr-Based Metal−Organic Frameworks: From Nano to Single Crystals. *Chem. - Eur. J.* **2011**, *17* (24), 6643−6651.

(46) Diring, S.; Furukawa, S.; Takashima, Y.; Tsuruoka, T.; Kitagawa, S. Controlled Multiscale Synthesis of Porous Coordination Polymer in Nano/Micro Regimes. *Chem. Mater.* **2010**, *22* (16), 4531−4538.

(47) Ringe, E.; Van Duyne, R. P.; Marks, L. D. Kinetic and Thermodynamic Modified Wulff Constructions for Twinned Nanoparticles. *J. Phys. Chem. C* **2013**, *117* (31), 15859−15870.

(48) Johnstone, D. N.; Crout, P.; Laulainen, J.; Høgås, S.; Martineau, B.; Bergh, T.; Smeets, S.; Collins, S.; Morzy, J.; Ånes, H.; Prestat, E.; Doherty, T.; Ostasevicius, T.; Danaie, M.; Tovey, R. *Pyxem/Pyxem: Pyxem 0.10.0*; Zenodo, 2019; DOI: 10.5281/zenodo.3533653.

(49) Pawley, G. S. Unit-Cell Refinement from Powder Diffraction Scans. *J. Appl. Crystallogr.* **1981**, *14* (6), 357−361.

(50) Coelho, A. A. TOPAS and TOPAS-Academic: An Optimization Program Integrating Computer Algebra and Crystallographic Objects Written in C++. *J. Appl. Crystallogr.* **2018**, *51* (1), 210−218.